JOURNAL OF THERMOPHYSICS AND HEAT TRANSFER
Vol. 23, No. 4, October–December 2009

Nonequilibrium Calculation of High-Temperature Radiating H_2-He Flowfield

Michiko Furudate*
Tohoku University, Sendai 980-8579, Japan

DOI: 10.2514/1.43961

Chemical kinetics of high-temperature hydrogen–helium gas mixture behind a shock wave is numerically investigated by integrating rate equations for species concentration in time. State-to-state transition rates are used to determine quasi-steady-state rate coefficients for atomic hydrogen ionization. The electron concentrations in front of the shock wave are deduced by solving the radiative heat transfer equation of molecular hydrogen. The computed incubation time of avalanche ionization is compared with the experimental data and those appeared in past studies. It is found that the precursor photoionization and the associative ionization of the molecular hydrogen are important to determine the ionization time behind the shock wave. The present chemical kinetic models are found to reproduce the shock tube experimental data of the ionization time reasonably well.

Nomenclature

$A(i,j)$	=	probability for the transition from upper state i to lower state j, 1/s
$B(i,j)$	=	rate coefficient for radiative transition from lower state i to upper state j, 1/s
B_λ	=	Planck function at wavelength λ, W/cm^2 · sr · μm
c_p	=	specific heat at constant pressure, J/K
E_{e^-}	=	electron energy, J/m^3
$E_H(i)$	=	energy level of state i of atomic hydrogen, J
h	=	enthalpy, J/kg
h_{f_s}	=	formation enthalpy of species s, J
I_{p_λ}	=	flux of photon at wavelength λ, 1/m^3 · s
I_λ	=	radiative intensity at wavelength λ, W/cm^2 · sr · μm
k	=	Boltzmann constant
k_f	=	collisional ionization rate coefficient, m^3/s
k_r	=	collisional three-body recombination rate coefficient, m^6/s
l	=	directional cosine
m	=	highest bound state quantum number
m_s	=	mass of a species s particle, kg
$N_H(i)$	=	number density of atomic hydrogen in state i, 1/m^3
N_s	=	number density of species s, 1/m^3
P	=	power absorbed by the Lyman α line, W/m^3
p	=	static pressure, Pa
R_s	=	production rate of species s, 1/m^3 · s
T	=	translational temperature of heavy particles, K
T_{e^-}	=	electron temperature, K
t	=	time, s
U_s	=	shock velocity, km/s
u	=	velocity, m/s
X_s	=	mole fraction of species s
Y_s	=	mass fraction of species s
x	=	x coordinate, m
α	=	collisional–radiative recombination rate coefficient, m^3/s
$\beta(i)$	=	rate coefficient for radiative recombination into state i, 1/s
ε_c	=	Lyman continuum radiation fraction
ε_L	=	Lyman α absorption factor
θ_s	=	ionization energy of spices s, J
κ_λ	=	absorption coefficients at wavelength λ, 1/cm
λ	=	wavelength, Å
μ	=	reduced mass, kg
$\bar{\nu}$	=	sum of collision frequency divided by mass of a particle, 1/s · kg
ν_{e^-s}	=	elastic collision frequency between electrons and the other species s, 1/s
ρ	=	density, kg/m^3
σ_{p_λ}	=	photoionization cross section at wave length λ, m^2
σ_λ	=	absorption cross section at wave length λ, cm^2
∇q_{rad}	=	divergence of radiative heat flux, W/m^3

Subscripts

E	=	equilibrium state
e^-	=	electron
s	=	species
1	=	state in front of a shock wave
2	=	state behind a shock wave
*	=	excited state

Presented as Paper 2008-3934 at the 40th Thermophysics Conference, Seattle, WA, 23–26 June 2008; received 21 February 2009; revision received 29 May 2009; accepted for publication 15 June 2009.

*Assistant Professor, Department of Aerospace Engineering; furu@cfd.mech.tohoku.ac.jp. Member AIAA.

I. Introduction

THE Galileo probe entered into Jupiter's atmosphere in 1995. To protect the probe from severe radiative heating during the entry flight, the surface of the Galileo probe was covered with ablative heat shield. The surface recession data were successfully obtained along the Galileo probe's entry flight trajectory [1,2]. The flight data have shown a surprisingly low surface recession in the stagnation region, with unexpectedly larger surface recession along the frustum region.

The flight data obtained in the entry flight of Galileo probe offer a unique opportunity to validate computational fluid dynamics (CFD) codes for predicting the aeroheating environment of the entry flows in future outer planetary missions. Because most of the outer planets in our solar system have an atmosphere similar to Jupiter's, which mainly consists of hydrogen and helium, all CFD codes for such purpose should be able to reproduce the flight data of the Galileo probe's entry flight. The larger surface recession along the frustum region of the probe was successfully explained by the injection-induced turbulence model [3,4]. However, the lower surface recession in the stagnation region has not yet been completely reproduced by CFD.

Park [5] has speculated earlier that the thermochemical nonequilibrium could explain such low heating rate in the stagnation region. Because radiative heating from ionized hydrogen is dominant in the shock layer, the narrower ionization region due to the nonequilibrium effect could lower the heating rate at the stagnation point.

Emission measurements in a shock tube by Leibowitz indicated that the ionization of atomic hydrogen had a finite incubation time [6]. In the study of Howe [7], an empirical formula based on the data of Leibowitz [6] was derived, and it was predicted that the un-ionized region could be half of the shock layer thickness for the flow condition at the maximum heating point along the Galileo probe's entry trajectory. However, Leibowitz and Kuo concluded that the radiative heating reduction was not significant even though they modeled the nonequilibrium ionization [8]. The reduction of radiative heat flux they obtained was less than 15%.

In the work of Liebowitz and Kuo [8], a two-step excitation–ionization reaction model was employed to describe the incubation time of electron-impact ionization. The model assumes that the atomic hydrogen in the first excited state is produced by collisions with atoms as the first step, and immediately ionized by the consequent collision as the second step. When the electron number density reaches the threshold value, the electron-impact ionization is triggered. In their work, the rate coefficients for the first step of the excitation–ionization reaction were determined to produce a radiative intensity profile behind a shock wave experimentally obtained in their electric arc shock tube. However, their rate coefficients seem to have some uncertainties in that they ignore the effect of the photoionization process. According to Bogdanoff and Park [9], the strong radiation from the driver gas possibly photoionizes the test gas before arrival of the shock wave, which can promote the initiation of electron-impact ionization. Moreover, radiation traveling upstream from the downstream side of the shock wave can photoionize the molecular hydrogen.

Recently, Park [5] has suggested new schematics of nonequilibrium hydrogen flow including the precursor photoionization of molecular hydrogen as follows. Precursor photoionization due to radiation from the shock layer causes the birth of electrons in front of the shock. Besides the photoionization of molecular hydrogen, rotational–vibrational excitation and dissociation of molecular hydrogen proceed behind the shock wave. When the electron number density and the electron temperature reach certain threshold values, the electron-impact ionization of atomic hydrogen suddenly becomes significant through an avalanche process. To estimate the thickness of the ionization region, we need to identify these threshold values quite accurately. For this purpose, the coupled rotational–vibrational relaxation process for molecular hydrogen was modeled by an analytical formula using the quasi-classical-trajectory approach in [10]. For the atomic hydrogen ionization, rate coefficients were derived by a classical approach and tabulated in [11]. The rate coefficients accounted for the effect of the Lyman line absorption by atomic hydrogen.

In a previous study [12], CFD calculations were carried out for flow conditions chosen along the entry trajectory of the Galileo probe using the latest nonequilibrium chemical models [10,11]. For the flow conditions at higher altitude, the un-ionized region was computed to be about 1 cm, and the subsequent ionized region was reduced to two-thirds of that obtained in an equilibrium calculation. However, the corresponding reduction of radiative heat flux toward the body surface was less than 10% at higher altitudes, and the radiative heat flux eventually coincided with that of equilibrium calculation at the peak heating point.

In the present study, we revisit the nonequilibrium calculation of high-temperature radiating hydrogen–helium mixture gas by using a more fundamental and precise approach that can account for the basic features of the new nonequilibrium chemical processes suggested by Park [5]. A set of rate equations for species concentrations is integrated in time. The rotational–vibrational excitation process is ignored in the present study for simplicity. The electronic excitations through heavy particle collisions are also ignored. Quasi-steady-state reaction rate coefficients, which can be calculated from the state-to-state transition rates, are employed for electron-impact ionization of atomic hydrogen. Radiative chemical processes such as photoionization or photodissociation of molecular hydrogen are also taken into account. To estimate the amount of electrons in front of the shock wave, the radiative heat transfer equation is solved for the flowfield including the precursor heating region. The obtained incubation time of the avalanche ionization is compared with those suggested in the past experimental and numerical studies.

II. Method of Calculation

A. Chemical Reaction Processes and Rate Coefficients

In the present calculation, seven chemical species of H_2, H_2^+, H, H^+, He, He^+, and e^- are considered. We employ the following chemical reaction processes:

Reaction 1 (R1)

$$H_2 + M \leftrightarrow H + H + M$$

Reaction 2 (R2)

$$H + e^- \leftrightarrow H^+ + e^- + e^-$$

Reaction 3 (R3)

$$He + e^- \leftrightarrow He^+ + e^- + e^-$$

Reaction 4 (R4)

$$H_2^+ + e^- \leftrightarrow H + H$$

Reaction 5 (R5)

$$H_2 + h\nu \rightarrow H_2^+ + e^-$$

Reaction 6 (R6)

$$H_2 + h\nu \rightarrow H + H^+ + e^-$$

The rate coefficients of the electron-impact ionization of atomic hydrogen in R2 are given by the source code provided in [11] under quasi-steady-state assumption. The rate coefficients include the following processes:

R2′

$$H(i) + e^- \leftrightarrow H^+ + e^- + e^-$$

R2″

$$H(i) + e^- \leftrightarrow H(i') + e^-$$

The source code in [11] outputs the parameters k_f, k_r, α, and $\beta(i)$ as a result of inputting N_H, N_{e^-}, T_{e^-}, and ε_L. The Lyman line absorption factor is defined by

$$\varepsilon_L = \frac{B(1,2)}{B(1,2)_E} = \frac{P/1.634\times 10^{-18} N_H(1)}{2^2 \exp[-E_H(2)/kT_{e^-}]A(2,1)} \tag{1}$$

where the power absorbed by the Lyman α line can be written by

$$P = 1.634\times 10^{-18} A(2,1) N_H(2) - \nabla q_{\text{rad}} \tag{2}$$

The divergence of radiative heat flux ∇q_{rad} in Eq. (2) is determined by solving the radiative heat transfer equation. From the output parameters, the change of electron number density due to the electron-impact ionization of atomic hydrogen is given by

$$\left(\frac{dN_{e^-}}{dt}\right)_{R2} = k_{fR2} N_H N_{e^-} - N_{e^-}^2 \alpha_1 - N_{e^-}^2 \varepsilon_c \beta(1) \tag{3}$$

$$\alpha_1 = \alpha - \beta(1) = N_{e^-} k_{rR2} + \sum_{i=2}^{m} \beta(i) \tag{4}$$

In the present calculation, m is taken to be 20.

The reaction rates both for photoionization in R5 and photodissociation in R6 can be written by

$$k_{fR5,R6} = \int \sigma_{p_\lambda} I_{p_\lambda} \, d\lambda \tag{5}$$

From the total ionization cross section for molecular hydrogen given in [13], the cross section for each R5 and R6 is determined by using the H^+/H_2^+ ratio given in [14]. The photon flux is calculated by solving the radiative heat transfer equations.

The expression of chemical reaction rates for the rest reaction processes are summarized in Table 1. The equilibrium constants are calculated by using the chemical equilibrium with application (CEA) program [16] to evaluate backward reactions for R1, R4, R5, and R6. The postshock temperatures in the present conditions are much higher than the applicable temperature range of the CEA program. However, it is believed that the effects of the equilibrium constants on the postshock flowfields in the present calculations are insignificant from the following perceptions: 1) the dissociating region is so short that it is almost negligible when compared to the ionization distance, and 2) ionization of helium and photoionizations of molecular hydrogen are insignificant in the high-temperature postshock flowfield.

B. Basic Equations for Thermochemical Kinetics and Flowfield

The changing rate of concentration N_s/ρ for species s is written by

$$\frac{\mathrm{d}}{\mathrm{d}t}\left(\frac{N_s}{\rho}\right) = \frac{R_s}{\rho} \tag{6}$$

Equation (6) is solved only for H_2^+, H, He^+, and e^-. The concentrations of other species are obtained by assuming that the elemental atomic number ratio is conserved. The time evolution of Eq. (6) is carried out by a fourth-order Runge–Kutta method with adaptive step-size control.

The flow properties behind a shock wave in the shock-fixed coordinate system are governed by the continuity equation, the momentum equation, and the energy equations, which are given by

$$\rho_1 u_1 = \rho_2 u_2 \tag{7}$$

$$p_1 + \rho_1 u_1^2 = p_2 + \rho_2 u_2^2 \tag{8}$$

and

$$h_1 + \tfrac{1}{2}u_1^2 = h_2 + \tfrac{1}{2}u_2^2 \tag{9}$$

The electron energy equation is given by

$$\frac{\partial}{\partial x}(E_{e^-}u) = 3N_{e^-}m_{e^-}\bar{\nu}k(T - T_{e^-}) - (\theta_H R_{H\mathrm{R2}} + \theta_{\mathrm{He}}R_{\mathrm{HeR3}}) \tag{10}$$

where the first term of the right-hand side describes the energy relaxation by elastic collisions, and the second term describes the energy loss due to electron-impact ionizations. Here, the sum of collision frequency $\bar{\nu}$ is defined by

$$\bar{\nu} = \sum_{s\neq e^-} \nu_{e^- s}/m_s$$

By applying the approximation that appears in [6], that is,

$$\frac{\partial}{\partial x}(E_{e^-}u) = 3N_{e^-}m_{e^-}\bar{\nu}k(T - T_{e^-}) - \theta_H[k_{f\mathrm{R2}}N_H - k_{f\mathrm{R2}}N_{H^+}N_{e^-}]N_{e^-} - \theta_{\mathrm{He}}[k_{f\mathrm{R3}}N_{\mathrm{He}} - k_{f\mathrm{R3}}N_{\mathrm{He}^+}N_{e^-}]N_{e^-} = 0 \tag{11}$$

the electron temperature can be determined as

$$T_{e^-} = \frac{T - [\theta_H(N_H b_{f\mathrm{R2}} - N_{H^+}N_{e^-}b_{b\mathrm{R2}}) + \theta_{\mathrm{He}}(N_{\mathrm{He}}b_{f\mathrm{R3}} - N_{\mathrm{He}^+}N_{e^-}b_{b\mathrm{R3}})]/3m_{e^-}\bar{\nu}k}{1 + [\theta_H(N_H a_{f\mathrm{R2}} - N_{H^+}N_{e^-}a_{b\mathrm{R2}}) + \theta_{\mathrm{He}}(N_{\mathrm{He}}a_{f\mathrm{R3}} - N_{\mathrm{He}^+}N_{e^-}a_{b\mathrm{R3}})]/3m_{e^-}\bar{\nu}k} \tag{12}$$

where we further assume that the forward and the backward reaction rates can be approximated by linear functions, $k_f = a_f T_{e^-} + b_f$ and $k_b = a_b T_{e^-} + b_b$. Once the electron temperature is determined, values of translational temperature, density, pressure, flow velocity, and enthalpy at the local time are then calculated from Eqs. (7–9) and the equations of state

$$p = \sum_{s\neq e^-} N_s kT + N_{e^-}kT_{e^-} \tag{13}$$

$$h = \sum_{s\neq e^-} Y_s c_{p_s} T + Y_{e^-}c_{p_{e^-}}T_{e^-} + \sum_{s\neq e^-} Y_s h_{f_s} \tag{14}$$

C. Radiative Heat Transfer

The radiative transfer equations are solved using the tangent-slab 1-D approximation [17], that is,

$$l\frac{\partial I_\lambda}{\partial x} = \kappa_\lambda(B_\lambda - I_\lambda) \tag{15}$$

The chemical species considered in the radiation calculation is H and H^+. A multiband model is used to evaluate the absorption coefficients. The absorption coefficient of the gas at wavelength λ is given by

$$\kappa_\lambda = N_H\sigma_\lambda^H + N_{H^+}\sigma_\lambda^{H^+} \tag{16}$$

The number of wavelength points is 1170 between 300 to 30000 Å. The Lyman line absorption factor ε_L and Lyman radiation fraction ε_c are evaluated at wavelength points in the range from 1210 to 1220 Å for the Lyman line, and from 300 to 975 Å for the Lyman continuum. The molecular hydrogen photoionization rate is conveniently determined by solving the radiative transfer equations twice. The photoionization absorption coefficient of the molecular hydrogen is accounted for together with those for H and H^+ in the first solution, whereas the absorption coefficients only for H and H^+ in the second solution. The production rate of electron by the photoionization is determined by the difference of absorbed energy between these two results.

III. Test Conditions

A. Test Flow Conditions

The present model is examined for the shock tube experimental conditions of Leibowitz [6]. The experiments were conducted in arc driven shock tubes, and the ionization distances behind the shock wave were determined from the measured radiation emission profiles. The static pressure and the shock velocity of the test cases are summarized in Table 2. The initial electron temperature behind the shock wave is set to be equal to the translational temperature.

Table 1 Reaction rate coefficients used in the present study

	Reaction	Reaction rates, m^3/s	Ref.
R1	$H_2 + He \rightarrow H + H + He$	$6.93\times10^{-12}/T\exp(-52,340/T)$	[6]
	$H_2 + H_2 \rightarrow H_2 + H + H$	$2.5k_{H_2+He\rightarrow H+H+He}$	[6]
	$H_2 + H \rightarrow H + H + H$	$20.0k_{H_2+He\rightarrow H+H+He}$	[6]
	$H_2 + H^+ \rightarrow H + H + H^+$	$20.0k_{H_2+He\rightarrow H+H+He}$	[6]
	$H_2 + e^- \rightarrow H + H + e^-$	$20.0k_{H_2+He\rightarrow H+H+He}$	[6]
R2	$H + e^- \rightarrow H^+ + e^- + e^-$	Source code in [11]	[11]
R3	$He + e^- \rightarrow He^+ + e^- + e^-$	$3.56\times10^{-23}\sqrt{8kT_{e^-}/\pi\mu_{e^-}}\exp(-285,248/T_{e^-})$	[6]
R4	$H_2^+ + e^- \rightarrow H + H$	$1.2\times10^{-16}(T_{e^-}/300)^{-0.4}$	[15]
	$H(3) + H \rightarrow H_2^+ + e^-$	$6.8\times10^{-18}T^{0.61}\exp(-13,000/T)$	[15]

Table 2 Test cases

Case	p_1, torr	U_s, km/s	X_{H2}	X_{He}
1-1	0.25	18.5	0.21	0.79
1-2	0.25	20.0	0.21	0.79
1-3	1.0	13.0	0.21	0.79
1-4	1.0	13.7	0.21	0.79
1-5	1.0	15.5	0.21	0.79
1-6	1.0	17.0	0.21	0.79
1-7	1.0	18.5	0.21	0.79
1-8	1.0	20.0	0.21	0.79
1-9	2.0	13.0	0.21	0.79
1-10	2.0	13.7	0.21	0.79
2-1	1.0	28.0	0.85	0.15
2-2	1.0	30.0	0.85	0.15
2-3	1.0	34.0	0.85	0.15
2-4	1.0	38.0	0.85	0.15
2-5	4.0	25.0	0.85	0.15
2-6	4.0	26.0	0.85	0.15
2-7	4.0	27.0	0.85	0.15
2-8	4.0	28.0	0.85	0.15

B. Computational Procedures

Schematics of the present computational model are shown in Fig. 1. In the present study, a fluid particle is traced by the Lagrangian method to determine flow properties, whereas the radiative heat transfer equations are solved by the Eulerian method.

The calculations are carried out in the following procedures. At first, we assume a stationary shock wave for a given upstream state. The fluid state just behind the shock wave can be found from the shock relation. Using this postshock state as the initial condition, the evolution of the fluid particle starting from the shock wave location is computed by the Lagrangian method. The location of a fluid particle is determined by integrating $dx/dt = u$ in time. Equation (6) is simultaneously integrated to determine chemical compositions of the fluid particle. Using the so-determined chemical compositions, the flow properties at the local time are calculated by solving Eqs. (7–9) and (12–14). When the fluid particle passes a computational mesh point, the local value of flow properties are stored to obtain the spatial distributions of the properties in the Eulerian coordinates. The time integration is terminated when the fluid particle reaches the boundary of computational domain.

Then, the radiative heat transfer equations are solved in both upstream and downstream regions of the shock wave simultaneously. Once the spatial distributions of photoionization rates and radiative absorption factors ε_1 and ε_c are determined from the radiative field, a fluid particle is placed at the boundary of the precursor region and its evolution toward the shock wave is solved by the Lagrangian method. Equation (6) is integrated in time to obtain the electron number density at the shock wave. The electron temperature is assumed to be the same as the constant translational temperature in the upstream region. It needs to be mentioned that the upstream state of the shock wave should be altered due to chemical reactions caused by absorption of radiation from the high-temperature region behind the shock wave. However, the assumption of constant pressure, temperature, and velocity is kept in the present study because the electron number density is very small.

Again, a fluid particle is released from the shock wave location, and the flow properties are obtained by the Lagrangian method using the local value of ε_L and ε_c at the location of fluid particle. For this time, the number density of electrons taken from the solution of the upstream side is given as part of the initial condition for a fluid particle. The electron temperature behind the shock wave is assumed to be same as the translational temperature behind the shock wave. When the flow properties behind the shock wave are determined, the radiative transfer equation is then solved. By continuing these computations iteratively, the converged flowfield in both upstream and downstream regions of the stationary shock wave is obtained.

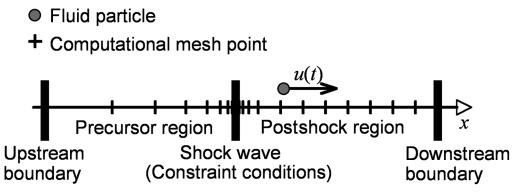

Fig. 1 Schematics of fluid particle and computational domain.

C. Determination of Ionization Time and Distance

The ionization time in the present study is defined by the so-called *e*-folding time. The precise definition employed in this study is given by

$$\frac{N_{e^-E} - N_{e^-2}(t)}{N_{e^-E} - N_{e^-2}(0)} = \frac{1}{e} \tag{17}$$

where N_{e^-E}, $N_{e^-2}(0)$, and $N_{e^-2}(t)$ denote the electron number density in equilibrium state, that behind the shock wave at $t = 0$, and that behind the shock wave at the ionization time t, respectively. The ionization distance in the present study is defined as a product of the *e*-folding ionization time and the shock velocity.

D. Computational Mesh System for Solving Radiative Transfer Equations

A schematic of the computational mesh system is illustrated in Fig. 1. The lengths of postshock computational domain are set to be between 3 and 5 times the ionization distances. The number of mesh points in the postshock computational domains is taken to be between 101 and 151. The length of the precursor region is set to be 2.0 m and is discretized by 121 mesh points for all cases considered in this study. Mesh points are clustered in the space near the shock wave to attain sufficient resolution. In the precursor region, the mesh interval is assumed to be a constant interval in logarithmic space. In the postshock region, a constant mesh interval in linear scale is chosen, except for the region very near the shock wave where a constant interval in logarithmic scale is assumed to attain the spatial accuracy for resolving the dissociation reaction of molecular hydrogen.

IV. Results

A. Fundamental Characteristics of Postshock Flowfield

The computed time evolutions of species number densities in the postshock flow for case 1-5 are presented in Fig. 2. The *e*-folding ionization time deduced from the time evolution of electron number density is determined to be 9.8 μs for this case. Hereafter, we call the time period before the ionization time the "un-ionized period" and after the ionization time the "ionized period." In Fig. 2, the number density of atomic hydrogen increases immediately due to the dissociation reaction of molecular hydrogen. The electron number density is shown to trace the time evolution of H_2^+ at first, and then to trace that of H^+. This indicates that the ionization of molecular hydrogen precedes the ionization of atomic hydrogen. The electron

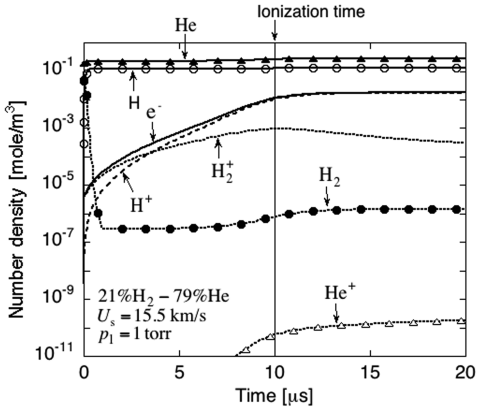

Fig. 2 Time evolution of species number density for case 1-5.

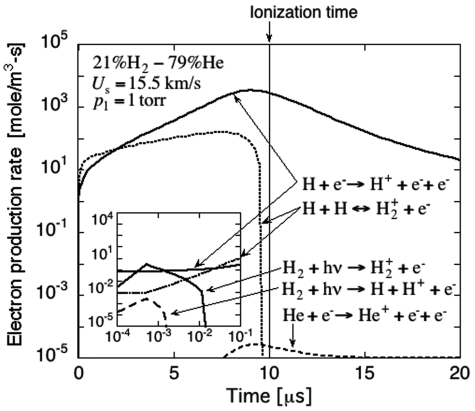

Fig. 3 Reaction specific electron production rates for case 1-5.

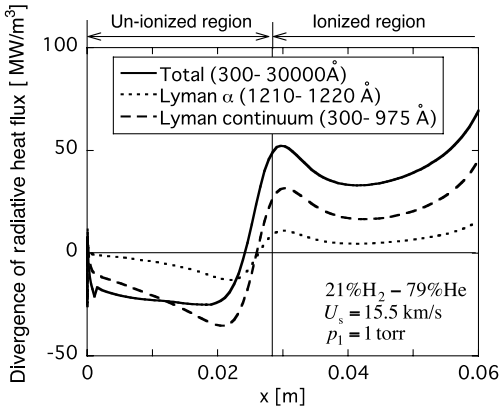

Fig. 5 Divergence of radiative heat flux in the postshock region for case 1-5.

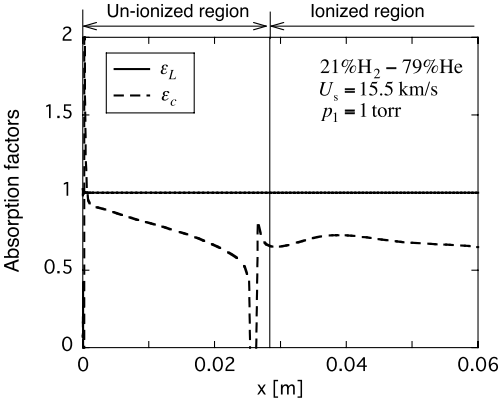

Fig. 6 Absorption factors for calculating atomic hydrogen ionization rate for case 1-5.

producing rate of chemical reactions from R2 to R6 are shown in Fig. 3. The inset figure in Fig. 3 shows the close-up view of electron production rate distribution immediately behind the shock wave, where the horizontal and the vertical axis, respectively, indicate the time in seconds and the electron production rate in mole/$m^3 \cdot s$. Throughout the un-ionized period, the electron-impact ionization reaction R2 and the associative ionization reaction R4 are dominant, whereas the photoionization reactions R5 and R6 are negligible. However, in the beginning phase of the un-ionized period, that is, from $t = 0.0$ to $t = 2$ μs, the associative ionization reaction contributes much to the production of electrons. Note that the electron production rate of the electron-impact ionization reaction R2 in the period from $t = 0$ to $t = 0.01$ μs is almost constant, whereas that of the associative ionization begins to increase quite rapidly. This confirms that electrons produced by the associative ionization reaction trigger the electron-impact ionization reaction R2.

The computed time evolutions of temperatures in the postshock flow for case 1-5 are shown in Fig. 4. The electron temperature is much lower than the translational temperature in the un-ionized period. This is because electron kinetic energy is consumed to remove electrons from atoms in the electron-impact ionization reactions.

In Fig. 5, the calculated divergence of radiative heat flux in the postshock region is displayed. The negative values of divergence in the un-ionized region imply that the gas is heated by radiative heat absorption in this region. In the ionized region where the divergence of radiative heat flux has positive values, the gas is cooled by radiative heat emission. It is also shown in Fig. 5 that a significant portion of the absorption is contributed by Lyman α line and Lyman continuum in the un-ionized region.

From the calculated radiative absorption, the Lyman α absorption factor ε_L and the continuum absorption factor ε_c for calculating atomic hydrogen ionization rate coefficients are determined. Figure 6 shows the distribution of ε_L and ε_c in the postshock flow. The value of ε_L is almost constant at one in the postshock region except immediately behind the shock wave. The values of ε_c are less than one in most parts of the postshock region. Note that the effect of this small ε_c on the ionization rate is insignificant, because the radiative recombination rates are about 1/100 of the collisional recombination rates in the present cases.

The characteristics of the postshock flowfields for the other cases are found to be similar to those of case 1-5, and therefore are not shown here.

B. Precursor Photoionization

In the present study, precursor ionization due to the absorption of radiation from the postshock flow is taken into account. Figure 7 shows the calculated photoionization rate in the precursor region for

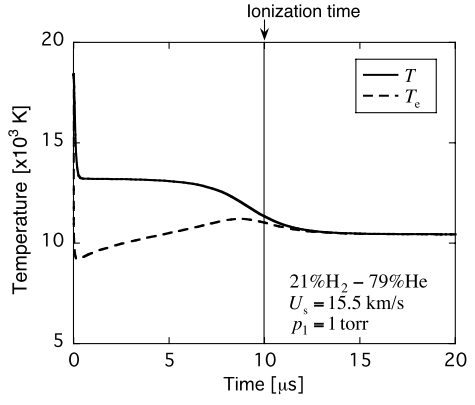

Fig. 4 Time evolution of temperatures for case 1-5.

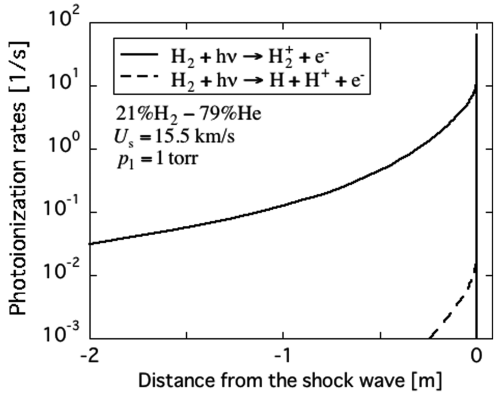

Fig. 7 Calculated photoionization rate in the precursor region.

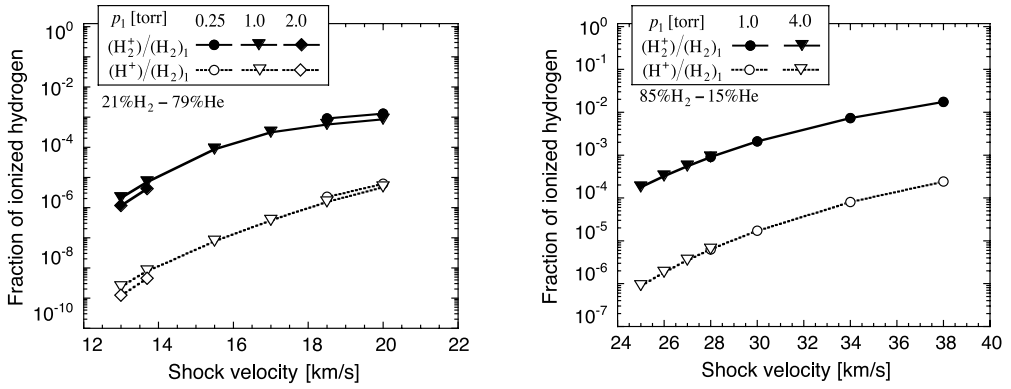

a) 21%H_2-79%He **b) 85%H_2-15%He**

Fig. 8 Fraction of ionized hydrogen in front of shock wave.

case 1-5. The photoionization rates are intense at the shock front and monotonically decrease toward upstream. By solving the rate equations for reactions R4–R6 using these photoionization rates, the electron number density in front of the shock wave is determined. Figure 8 summarizes the so-obtained normalized number densities of H_2^+ and H^+. For 21%H_2–79%He flows in cases 1-1–1-10, the degree of photoionization in the precursor region is relatively low. Only 0.1% of molecular hydrogen is ionized in the highest shock velocity case. For 85%H_2–15%He flows in cases 2-1–2-8, the degree of photoionization raises up to 0.9% when the shock velocity becomes as high as 38 km/s. The effect of the precursor photoionization on the ionization time behind the shock wave will be discussed in the following subsection.

In the present study, computational procedures are iteratively repeated until the computed flowfield converges. As shown in Fig. 9, only three to four iterations are needed for obtaining the convergence of electron number density in front of the shock wave for case 1-5.

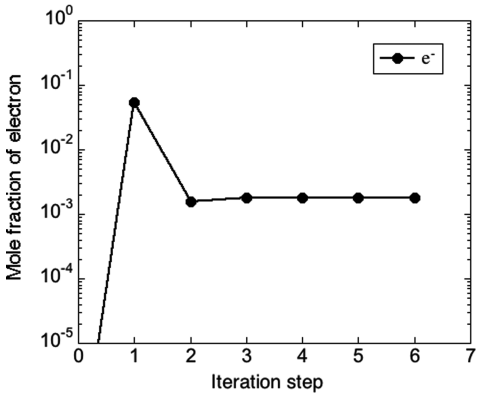

Fig. 9 Convergence history of electron mole fraction in front of shock wave.

C. Ionization Time

In Fig. 10, the present chemical kinetic models are validated against the shock tube experimental data of Leibowitz in terms of the ionization time and ionization distance. Generally, both the ionization time and ionization distance agree well with the experimental data. In the higher temperature cases indicated in Fig. 10a, the present ionization time is slightly longer than the experimental data. This tendency also appears in the higher shock velocity cases in Fig. 10b, where the present ionization distance is longer than the experimental data. According to Bogdanoff and Park [9], the driven gas can be photoionized by the driver gas "flash" in the arc-heated shock tube. If this is the case, the measured ionization time can be shorter than the present calculation in which such an effect is not considered. In Fig. 10b, the calculated ionization distance tends to be shorter than the experimental data in lower shock velocity cases. This may be caused by ignoring the internal energy relaxations of molecular hydrogen. According to [10], rotational–vibrational relaxation time of molecular hydrogen through H_2-H_2 collisions is about 2×10^{-8} atm · s at the postshock temperature of 25,000 K for a shock velocity of 25 km/s. This is equivalent to the relaxation distance of 23 torr · cm for pure hydrogen gas, which is in comparable order to the present ionization time.

To see the effect of precursor photoionization, the present results are compared with the computed results where photoionization processes are ignored. In Fig. 11, the effect of photoionization is shown to be significant for the higher shock velocity cases. Especially in cases 2-3 and 2-4, the calculated results agree with the experimental data when the precursor photoionization effect is taken into account.

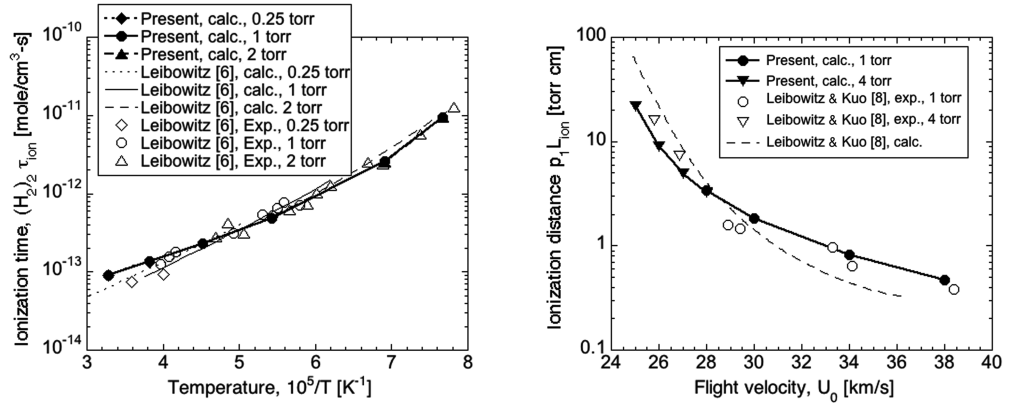

a) 21%H_2-79%He **b) 85%H_2-15%He**

Fig. 10 Ionization time and ionization distance.

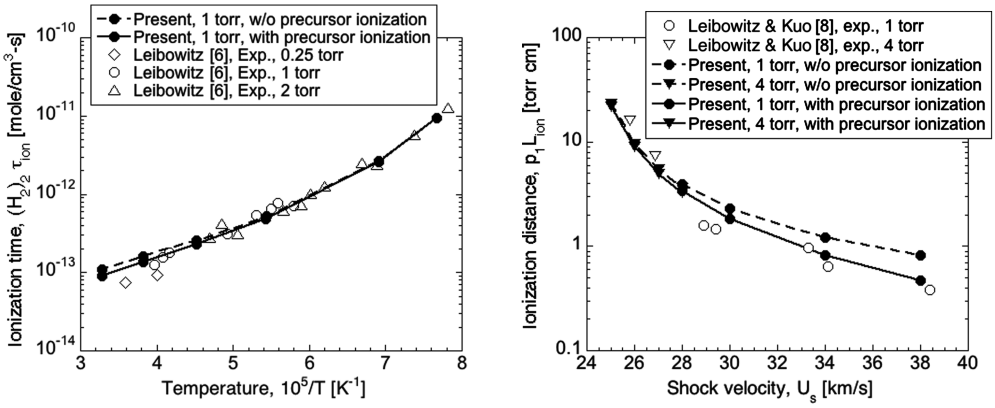

a) 21%H_2-79%He **b) 85%H_2-15%He**

Fig. 11 Effect of precursor ionization on ionization time/distance.

As shown in the previous subsection, the photoionization reactions are negligible in the postshock flow. Moreover, the absorption factors ε_L and ε_c are almost constant throughout the postshock flowfield. We therefore note that the present ionization time can be reproduced without solving the radiative transfer equations if the fraction of precursor ionization shown in Fig. 8 is given in advance as the input parameter.

The present calculations assume that the electron temperature behind the shock wave equals the translational temperature. An alternative assumption is examined to understand the effects of the electron temperature behind the shock wave on the ionization time. As the lower limiting case, the electron temperature behind the shock wave is set to be 298 K, which corresponds to the value of upstream electron temperature. Additional calculations with this assumption are carried out for cases 1-5, 2-1, and 2-8. Although figures are not shown, a very minor variation of the ionization time/distances are obtained by this assumption for cases 1-5 and 2-1 when compared with the calculations under the original electron temperature conditions. For case 2-8, the obtained ionization distance is shifted to the value calculated without precursor photoionizations. This is because the electron number density in front of the shock is reduced due to the low electron temperature behind the shock wave. The fraction of ionization hydrogen in front of the shock wave is about one-tenth of the value given by the calculation with the original electron temperature condition. These results suggest that an accurate electron temperature behind the shock wave is necessary for a precise prediction of ionization time when the precursor photoionization is significant. However, because the precursor photoionization is not so significant for the present cases, the effects of the electron temperature behind the shock wave is small enough to justify the validity of setting electron temperature equal to the translational temperature behind the shock wave.

D. Comparisons with the Two-Step Ionization Model

The present chemical kinetics in the postshock region for case 1-5 are compared with the results from the two-step ionization model by Leibowitz [6]. In Fig. 12a, the electron number densities start to increase after a certain incubation period in both results. However, the maximum gradient of the electron number density in the present calculation is much steeper than that given by the two-step model. As shown in Fig. 12b, the electron temperature obtained by the present model is much lower than that of the two-step model in the unionized period. Because the ionization reaction consumes electron energy, as indicated in Eq. (10), this lowered electron temperature implies that the larger amount of atoms are ionized in the present calculation. This can be confirmed by the electron number density distribution shown in Fig. 12a, in which the amount of electrons in the equilibrium region calculated by the present model is larger than that given by the two-step model. In Fig. 13, the calculated distributions of the radiative heat flux toward downstream are compared. It is shown that the radiative heat flux toward the downstream given by the present chemical kinetic model is less than half of that given by the two-step model. The lower electron temperature shown in Fig. 12b is probably the main cause of this lower radiative heat flux.

E. Effect of Computational Domain Size

Length of the computational domain can alter the solution of the radiative transfer equation and, consequently, the computed flowfield. In Fig. 14, the calculated electron density distributions for three different domain lengths are compared. The inset figure in Fig. 14a shows the close-up view of the calculated electron density distributions just in front of the shock wave, where the horizontal and the vertical axes, respectively, indicate the distance from the shock

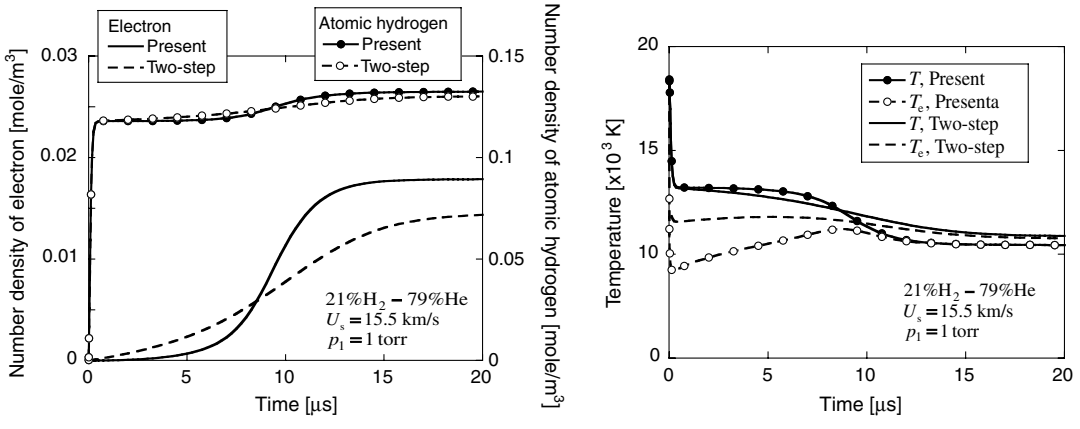

a) Number density of H and e **b) Temperatures**

Fig. 12 Comparisons of chemical kinetic models.

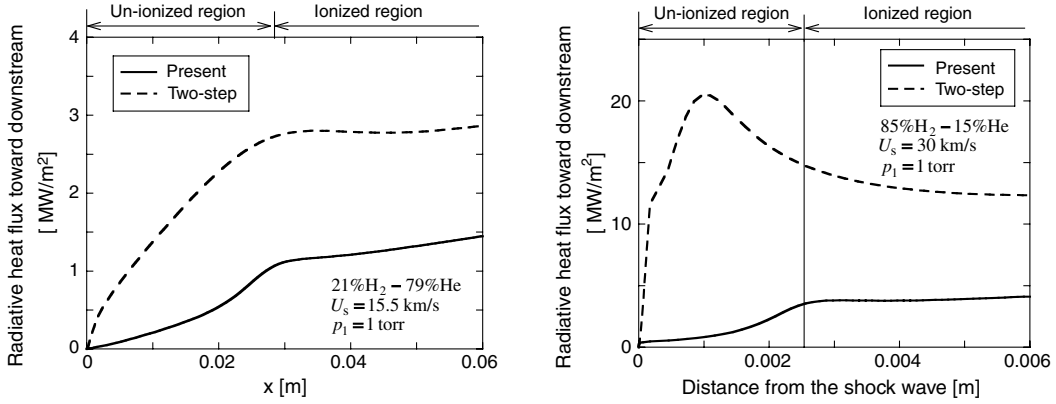

a) Case 1-5 b) Case 2-2

Fig. 13 Comparisons of radiative heat flux toward downstream.

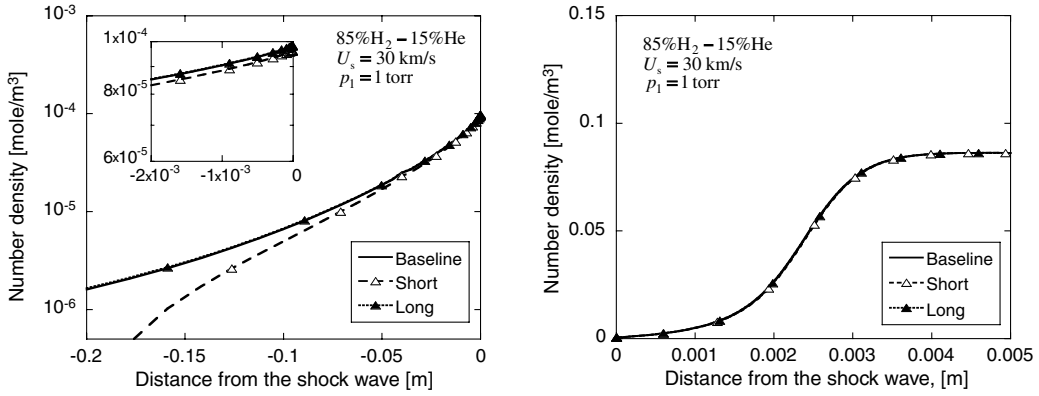

a) Precursor region b) Postshock region

Fig. 14 Effect of computational domain size in electron number density distribution.

and the number density of electrons. Table 3 summarizes these computational domains, called baseline, short, and long. The length of the baseline computational domain is shortened in the short domain and lengthened in the long domain, although the mesh spacing is the same for all the mesh systems. As shown in Fig. 14a, the calculated result with the short domain generally gives lower electron number density in the precursor region. On the other hand, the calculated electron number densities in front of the shock wave for different domain lengths reasonably agree each other. In the postshock region, the electron number density distribution calculated with these three mesh systems coincide each other, as seen in Fig. 14b. From these results, the computational domain size of the baseline mesh system turns out to be sufficient to predict the precursor ionization and the postshock flowfield.

F. Effect of Computational Mesh Fineness

To examine the grid convergence, calculations are carried out using three different mesh spacings as indicated in Table 4. They are named baseline, coarse, and fine. The length of the computational domain is the same for all of these meshes, but the coarse mesh has doubled mesh spacing and the fine mesh has halved mesh spacing of that for baseline mesh. The calculated electron number density distributions are compared in Fig. 15. In the precursor region, coarse mesh predicts slightly higher electron number density, whereas the fine mesh gives a reasonable agreement with that of the baseline mesh. In the postshock region, these mesh systems give the electron number density distributions similar to each other. From these results, one can say that the baseline mesh system can yield grid converged solutions.

V. Discussion

The chemical kinetic model studied in the present work successfully reproduces the shock tube experimental data of ionization time without any parameter correction. This is in contrast to Leibowitz's study [6,8], in which the rate coefficients for the excitation–ionization process of atomic hydrogen in the two-step model needed some corrections for reproducing his experimental results. In the present chemical kinetic model, those electrons to trigger the electron-impact ionization of atomic hydrogen are produced by the photoionization of molecular hydrogen in the precursor region and also by the associative ionization of molecular hydrogen in the postshock region. Photoionization seems to be

Table 3 Examined sizes of computational domain

	Precursor region		Postshock region	
	Length, m	Number of points	Length, m	Number of points
Baseline	2.0	120	0.0127	141
Short	0.20	100	0.00673	81
Long	20	140	0.0246	261

Table 4 Examined numbers of mesh points

	Precursor region		Postshock region	
	Length, m	Number of points	Length, m	Number of points
Baseline	2.0	120	0.0127	141
Coarse	2.0	50	0.0127	71
Fine	2.0	240	0.0127	281

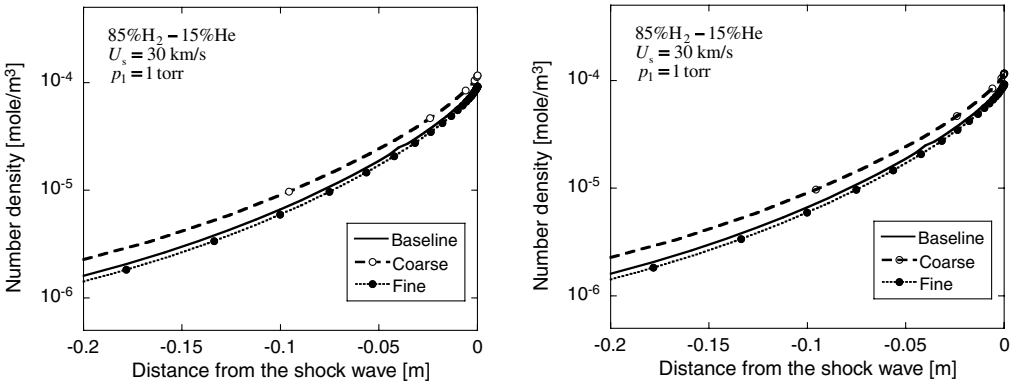

a) Precursor region **b) Postshock region**

Fig. 15 Effect of computational mesh fineness on electron number density distribution.

essentially important when the shock velocity is very high, especially in cases 2-3 and 2-4. Flow conditions in these cases correspond to that for the maximum heating point along the entry trajectory of the Galileo probe [1,2]. On the other hand, flow conditions in cases 2-1, 2-2, and 2-5–2-8 correspond to that for the entry flight into the atmosphere of Saturn with an entry velocity of 25–30 km/s. In cases 2-5–2-7, the ionization distances given by the present calculation tend to become shorter than the experimental data. This implies that the internal energy relaxation process of molecular hydrogen can have an important role when the fraction of molecular hydrogen in the freestream is high and the flight velocity is relatively low. Finally, we emphasize that the calculated radiative heat flux toward downstream using the present chemical kinetic model is less than half of that given by the two-step model. This result suggests the possibility that the present chemical kinetic model can explain the small amount of recession at the stagnation region in the flight data of the Galileo probe.

VI. Conclusions

A new set of chemical kinetic models is tested for the one-dimensional flowfield behind a shock wave in H_2-He mixture gas. The rate equations are solved using new rate coefficients of the atomic hydrogen ionization of Park [11]. The photoionization of molecular hydrogen in the precursor region is taken into account. It is found that the new set of chemical reactions reproduce the shock tube experimental data of the ionization time of the flowfield behind a shock wave. The associative ionization of molecular hydrogen as well as the photoionizations of a molecular hydrogen molecule has an important roll to initiate the electron-impact ionization of atomic hydrogen.

Acknowledgments

The author would like to express his appreciation to K. Sawada and N. Ohnishi, Tohoku University, Japan, and K. Fujita, Japan Aerospace Exploration Agency, for their valuable suggestions. The author also thanks C. Park, Korea Advanced Institute of Science and Technology, Korea, for providing the subroutine to determine the atomic hydrogen ionization rate coefficients, and S. Matsuyama, Japan Aerospace Exploration Agency, for providing the subroutine to solve the radiative heat transfer.

References

[1] Milos, F. S., "Galileo Probe Heat Shield Ablation Experiment," *Journal of Spacecraft and Rockets*, Vol. 34, No. 6, Nov.–Dec. 1997, pp. 705–713.
doi:10.2514/2.3293

[2] Milos, F. S., Chen, Y. K., Squire, T. H., and Brewer, R. A., "Analysis of Galileo Probe Heatshield Ablation and Temperature Data," *Journal of Spacecraft and Rockets*, Vol. 36, No. 3, May–June 1999, pp. 298–306.
doi:10.2514/2.3465

[3] Park, C., "Injection-Induced Turbulence in Stagnation Point Boundary Layers," *AIAA Journal*, Vol. 22, No. 2, Feb. 1984, pp. 219–255.
doi:10.2514/3.8371

[4] Matsuyama, S., Ohnishi, N., Sasoh, A., and Sawada, K., "Numerical Simulation of Galileo Probe Heatshield Ablation and Thermal Protection System," *Journal of Thermophysics and Heat Transfer*, Vol. 19, No. 1, 2005, pp. 28–35.
doi:10.2514/1.10264

[5] Park, C., "Heatshielding Problems of Planetary Entry, A Review," AIAA Paper 99-3415, June 1999.

[6] Leibowitz, L. P., "Measurements of the Structure of an Ionizing Shock Wave in a Hydrogen–Helium Mixture," *Physics of Fluids*, Vol. 16, No. 1, Jan. 1973, pp. 59–68.
doi:10.1063/1.1694174

[7] Howe, J. T., "Hydrogen Ionization in the Shock Layer for Entry into the Outer Planets," *AIAA Journal*, Vol. 12, No. 6, June 1974, pp. 875–876.
doi:10.2514/3.49371

[8] Leibowitz, L. P., and Kuo, T.-J., "Ionizational Nonequilibrium Heating During Outer Planetary Entries," *AIAA Journal*, Vol. 14, No. 9, Sept. 1976, pp. 1324–1329.
doi:10.2514/3.61465

[9] Bogdanoff, D. W., and Park, C., "Radiative Interaction Between Driver and Driven Gases in an Arc-Driven Shock Tube," *Shock Waves*, Vol. 12, No. 3, 2002, pp. 205–214.
doi:10.1007/s00193-002-0157-y

[10] Furudate, M., Fujita, K., and Abe, T., "Coupled Rotational-Vibrational Relaxation of Molecular Hydrogen at High Temperatures," *Journal of Thermophysics and Heat Transfer*, Vol. 20, No. 3, July 2006, pp. 457–464.
doi:10.2514/1.16323

[11] Park, C., "Effect of Lyman Radiation on Nonequilibrium Ionization of Atomic Hydrogen," AIAA Paper 2004-2277, 2004.

[12] Furudate, M., and Jeung, I. S., "Nonequilibrium Calculation of Flowfield over Galileo Probe," AIAA Paper 2006-0383, 2006.

[13] Yan, M., Sadeghpour, H. R., and Dalgarno, A., "Photoionization cross section of He and H2," *Astrophysical Journal*, Vol. 496, No. 2, Pt. 1, April 1998, pp. 1044–1050.
doi:10.1086/305420

[14] Chung, Y. M., Lee, E.-M., Masuoka, T., and Samason, J. A. R., "Dissociative Photoionization of H2 from 18 to 124 eV," *Journal of Chemical Physics*, Vol. 99, No. 2, July 1993, pp. 885–889.
doi:10.1063/1.465352

[15] Stanicil, P. C., Lepp, S., and Dalgarno, A., "The Deuterium Chemistry of the Early Universe," *Astrophysical Journal*, Vol. 509, No. 1, Pt. 1, Dec. 1998, pp. 1–10.
doi:10.1086/306473

[16] McBride, B. J., and Gordon, S., *Computer Program for Calculation of Complex Chemical Equilibrium Compositions and Applications, II: Users Manual and Program Description*, NASA Reference Publ. 1311, 1996.

[17] Matsuyama, S., Shimogonya, Y., Ohnishi, N., Sasoh, A., and Sawada, K., "Multiband Radiation Model for Simulation of Galileo Probe Entry Flowfield," *Journal of Thermophysics and Heat Transfer*, Vol. 20, No. 3, 2006, pp. 611–614.
doi:10.2514/1.16432